

EUROPEAN ORGANIZATION FOR NUCLEAR RESEARCH

CERN-PH-EP/2005-004
February 15, 2005

Measurement of the Photon Structure Function F_2^γ with the L3 Detector at LEP

L3 Collaboration

Abstract

The $e^+e^- \rightarrow e^+e^- h$ reaction, where one of the two electrons is detected in a low polar-angle calorimeter, is analysed in order to measure the hadronic photon structure function F_2^γ . The full high-energy and high-luminosity data set, collected with the L3 detector at centre-of-mass energies $189 \text{ GeV} \leq \sqrt{s} \leq 209 \text{ GeV}$, corresponding to an integrated luminosity of 608 pb^{-1} is used. The Q^2 range $11 \text{ GeV}^2 \leq Q^2 \leq 34 \text{ GeV}^2$ and the x range $0.006 \leq x \leq 0.556$ are considered. The data are compared with recent parton density functions.

Submitted to *Phys. Lett. B*

1 Introduction

Photons are ideal tools for probing the structure of more complex objects such as the proton in deep-inelastic scattering experiments. At LEP, in the $e^+e^- \rightarrow e^+e^-\gamma^*\gamma \rightarrow e^+e^-hadrons$ reaction, two virtual photons are produced by the incoming electrons¹⁾ and their interaction yields hadrons. If the scattering angle of one of the electrons, θ_{tag} , is sufficiently large, it is observed in the low polar-angle electromagnetic BGO calorimeter [1] of the L3 detector [2], originally devised to detect low angle Bhabha scattering in order to measure the LEP luminosity. This allows to measure the four-momentum, k' , of this “tagged” electron. For “single-tagged” events the second electron is undetected, its polar angle is small and the virtual photon radiated from this electron is quasi-real. In the framework of a deep-inelastic scattering formalism the process $e^+e^- \rightarrow e^+e^-hadrons$ is written as the convolution of the target photon flux with the reaction $e(k) + \gamma(p) \rightarrow e(k') + hadrons$. The photon, γ^* , with four-momentum $q = k - k'$ and a large virtuality $Q^2 = -q^2 \sim 2E_{tag}E_{beam}(1 - \cos\theta_{tag})$, is considered as a point-like probe investigating the structure of the target photon, γ , with four-momentum p and virtuality $P^2 = -p^2 \simeq 0$. E_{tag} is the energy of the tagged electron and E_{beam} the energy of the beam. The differential cross section is written in terms of the scaling variables $x = Q^2/(p \cdot q) = Q^2/(Q^2 + W_{\gamma\gamma}^2 + P^2)$ and $y = (q \cdot p)/(k \cdot p) = 1 - (E_{tag}/E_{beam} \cos^2\theta_{tag})$ as [3, 4]:

$$\frac{d\sigma_{e\gamma \rightarrow eX}(x, Q^2)}{dx dQ^2} = \frac{2\pi\alpha^2}{xQ^4} [(1 + (1 - y)^2) F_2^\gamma(x, Q^2) - y^2 F_L^\gamma(x, Q^2)] \quad (1)$$

The variable x depends on the two-photon centre-of-mass energy, $W_{\gamma\gamma}$, equal to the effective mass of the produced hadrons. The inelasticity y is small ($y < 0.3$) in the kinematic region of this study and consequently only $F_2^\gamma(x, Q^2)$ contributes appreciably to the cross section. By convention, F_2^γ/α is measured, where α is the fine-structure constant. Using this approach, the photon structure function has been extensively studied at low-energy e^+e^- colliders [5] and at LEP [5–7].

A virtual photon can interact as a point-like particle in “direct processes”; it can fluctuate into a vector meson (ρ, ω, ϕ) inducing soft hadronic interactions in “VDM processes” or it can interact via its partonic content of quarks or gluons in “resolved processes”. High Q^2 single-tag events favour perturbative QED and QCD diagrams such as $\gamma\gamma \rightarrow q\bar{q}$, $\gamma q \rightarrow gq$ or $\gamma g \rightarrow q\bar{q}$. The two resolved processes, $\gamma q \rightarrow gq$ and $\gamma g \rightarrow q\bar{q}$, are described using parton density functions extracted from the photon structure functions measured in previous experiments at PEP, PETRA and TRISTAN. Reviews of the existing parameterisations may be found in References 8 and 9. Recently, a new parametrisation was obtained adding published LEP data [10].

This analysis uses the 608.1 pb⁻¹ of high-energy LEP data, collected at e^+e^- centre-of-mass energies $189 \text{ GeV} \leq \sqrt{s} \leq 209 \text{ GeV}$. The data are grouped in four average \sqrt{s} values, presented in Table 1. These high-energy data allow to extend our previous measurements [6] at $\sqrt{s} \simeq 91 \text{ GeV}$ and $\sqrt{s} = 183 \text{ GeV}$ in the small- x region down to 0.006 and in the medium- x region up to 0.556 for the Q^2 range $11 \text{ GeV}^2 \leq Q^2 \leq 34 \text{ GeV}^2$. The $e^+e^- \rightarrow e^+e^-hadrons$ cross section and the F_2^γ photon structure function are studied as a function of x in the three Q^2 intervals $11 \text{ GeV}^2 \leq Q^2 \leq 14 \text{ GeV}^2$, $14 \text{ GeV}^2 \leq Q^2 \leq 20 \text{ GeV}^2$ and $20 \text{ GeV}^2 \leq Q^2 \leq 34 \text{ GeV}^2$. The Q^2 evolution of F_2^γ is also studied combining the values at $\langle Q^2 \rangle = 12.4, 16.7$ and 25.5 GeV^2 with our previous measurements.

¹⁾Throughout this Letter, the term “electron” indicates both electron and positron.

2 Monte Carlo Models

The value of the Q^2 variable is accurately determined by measuring the four-momentum of the scattered electron. However, the effective mass of the final state hadrons is only partially reconstructed, as these are often produced at low polar angles where no tracking system can be installed. A Monte Carlo modelling of the final state hadrons is therefore necessary [11] to determine the x variable.

Three Monte Carlo generators are used to model the process $e^+e^- \rightarrow e^+e^- \text{hadrons}$: PHOJET [12], PYTHIA [13] and TWOGAM [14].

PHOJET describes hadron-hadron, photon-hadron and photon-photon collisions. It is based on the Dual Parton Model combined with the QCD-improved parton model [15]. In order to have a continuous transition between hard and soft processes, the distribution of the transverse momentum, p_t , of the soft partons is matched to the one predicted by QCD. The two-photon luminosity is calculated from the flux of transversely polarised photons; corrections for the longitudinally polarised photons are thus incorporated into an effective two-photon cross section. The transition from real-photon to virtual-photon scattering is obtained by a change of the relative weight of all partial cross sections.

PYTHIA is a general purpose Monte Carlo. For two-photon interactions it incorporates leading order (LO) hard-scattering processes as well as elastic, diffractive and low p_t events. The classification of the photon interactions into three different components, direct, resolved and VDM, results in six different classes of events. Events are also classified according to the hard scales involved in the process: photon virtualities and parton transverse momenta.

TWOGAM generates three different processes separately: point-like photon-photon interactions, resolved processes, and non-perturbative soft processes described by the Generalised Vector Dominance Model (GVDM). The structure of the program is modular and the photon flux is calculated with an exact LO formula. The cross sections of the three different processes are adjusted to fit the x -distribution of the data. The cross section of the direct process is fixed to the value expected in our kinematic range, $\sigma = 41 \text{ pb}$. The QCD and the VDM cross sections are then adjusted to $\sigma = 5 \text{ pb}$ and $\sigma = 28 \text{ pb}$, respectively.

For the three Monte Carlo generators parton showering and hadronisation are described by JETSET [16]. The dominant backgrounds are evaluated with PYTHIA for $e^+e^- \rightarrow q\bar{q}(\gamma)$ and DIAG36 [17] for $e^+e^- \rightarrow e^+e^-\tau^+\tau^-$.

All Monte Carlo samples are generated with a luminosity at least five times greater than the experimental one. All events are passed through a full detector simulation which uses the GEANT [18] and GHEISHA [19] programs and takes into account detector efficiencies and time-dependent effects. Monte Carlo events are then reconstructed in the same way as the data.

3 Data Analysis

Events are mainly accepted by two independent triggers: the single-tag trigger and the central track-trigger. The single-tag trigger requires at least 70% of the beam energy to be deposited in one of the low polar-angle calorimeters, in coincidence with at least one track in the central tracking chamber. The central track-trigger requires at least two tracks back-to-back in the transverse plane within $\pm 60^\circ$, each with $p_t > 150 \text{ MeV}$. The average trigger efficiency is about 97%. There is a single-tag trigger signal for about 90% of the selected events and a central track-trigger signal for about 85% of the selected events.

3.1 Event Selection

Events are selected by requiring a single scattered electron in the low polar-angle calorimeter and a hadronic final state. A tagged electron candidate is the highest energy cluster with a shape consistent with an electromagnetic shower, $E_{\text{tag}}/E_{\text{beam}} > 0.7$, as shown in Figure 1a, and a polar angle in the fiducial region $0.0325 \text{ rad} \leq \theta \leq 0.0637 \text{ rad}$ inside the geometrical acceptance $0.030 \text{ rad} \leq \theta \leq 0.066 \text{ rad}$. To ensure that the virtuality of the target photon is small, the highest-energy cluster in the low polar-angle calorimeter opposite to the tagged electron must have an energy less than 20% of the beam energy, as shown in Figure 1b.

At least four additional particles must be detected. A particle can be a track or a photon. A track must have $p_t > 100 \text{ MeV}$ and a distance of closest approach in the transverse plane to the interaction vertex of less than 10 mm. A photon is a cluster in the electromagnetic BGO calorimeters with energy above 100 MeV, not associated with a charged track.

To reduce the background from the process $e^+e^- \rightarrow q\bar{q}(\gamma)$, the total energy deposited in the electromagnetic and hadronic calorimeters must be less than 40% of the center-of-mass energy, as shown in Figure 1c. The events with a large value of the total energy are due to the $e^+e^- \rightarrow Z\gamma \rightarrow q\bar{q}\gamma$ process, where the radiative photon is misidentified as the tagged electron.

The mass of the hadronic final state, W_{vis} , is calculated from all tracks and calorimetric clusters. Additional clusters detected in the low polar-angle calorimeter are assigned the pion mass and included in the calculation of W_{vis} . To avoid the hadronic resonance region, W_{vis} is required to be greater than 4 GeV, as presented in Figure 1d.

Figure 2 shows the Q^2 distribution for each \sqrt{s} sample. Only events with $11 \text{ GeV}^2 \leq Q^2 \leq 34 \text{ GeV}^2$ are studied. The number of selected events and the backgrounds from the $e^+e^- \rightarrow e^+e^-\tau^+\tau^-$ and $e^+e^- \rightarrow q\bar{q}(\gamma)$ processes are given in Table 1. The background is dominated by the $e^+e^- \rightarrow e^+e^-\tau^+\tau^-$ production. The contribution from the $e^+e^- \rightarrow \tau^+\tau^-$ and $e^+e^- \rightarrow W^+W^-$ processes is negligible. The background from beam-gas and beam-wall events is found to be negligible by inspection of the radial distribution of track intersections. The W_{vis} and $x_{\text{vis}} = Q^2/(Q^2 + W_{\text{vis}}^2)$ distributions are presented in Figure 3 for all selected data. The PYTHIA and TWOGAM model reproduce the data rather well, except at large values of W_{vis} . PHOJET presents a harder mass spectrum and predicts too many events for $x_{\text{vis}} < 0.1$ and is therefore not used in the following.

The total acceptance is calculated for each data sample separately. It takes into account the trigger efficiency, the geometrical acceptance and the selection cuts. An example is presented in Figure 4a for the data at $\sqrt{s} = 189 \text{ GeV}$.

4 Results

4.1 Unfolding and Differential Cross Sections

The cross section $\Delta\sigma/\Delta x$ as a function of x for the reaction $e^+e^- \rightarrow e^+e^- \text{hadrons}$ is measured for three Q^2 intervals: $11 \text{ GeV}^2 \leq Q^2 \leq 14 \text{ GeV}^2$, $14 \text{ GeV}^2 \leq Q^2 \leq 20 \text{ GeV}^2$ and $20 \text{ GeV}^2 \leq Q^2 \leq 34 \text{ GeV}^2$. Each data set is subdivided into bins of x_{vis} of similar statistics, as listed in Table 2. A Bayesian unfolding procedure [20] is used to relate the measured x_{vis} to the true value of x and to correct the data for the detector acceptance and efficiency. This procedure is applied using, in turn, the PYTHIA and TWOGAM generators. The average of the cross sections obtained in the two cases is retained. The correlation between the generated value of x and x_{vis} is similar for the two models. The one obtained with PYTHIA is shown in Figure

4b. The cross sections measured for each x interval of average value $\langle x \rangle$ and for each value of \sqrt{s} are given in Table 2 with their statistical and systematic uncertainties. The bin-to-bin correlation matrices obtained with PYTHIA and TWOGAM for $\sqrt{s} = 189$ GeV are shown in Tables 3 and 4, respectively. Similar matrices are obtained for the other values of \sqrt{s} .

4.2 Systematic Uncertainties

The systematic uncertainties on the cross sections are estimated for each data sample, for each x bin and for each Q^2 interval. Three main sources of systematic uncertainties are considered: the selection procedure, the trigger efficiency and the Monte Carlo model. Their average effects over the full data sample are listed in Table 5.

The uncertainties from the selection procedure are estimated by varying the selection cuts. The fiducial value of the polar angle in the low polar-angle calorimeter is varied from 0.0325 rad to 0.0360 rad and from 0.0637 rad to 0.060 rad. These changes result in a Q^2 -dependent uncertainty, as the highest and lowest values of the Q^2 are affected by the fiducial cut. The cut on E_{tag} is varied from $0.70E_{\text{beam}}$ to $0.65E_{\text{beam}}$ and $0.75E_{\text{beam}}$. The anti-tag cut is changed from $0.20E_{\text{beam}}$ to $0.15E_{\text{beam}}$ and $0.25E_{\text{beam}}$. The numbers of particles is varied from four to three and five. The cut on the total energy in the calorimeters relative to \sqrt{s} is varied from 0.40 to 0.35 and 0.45. The uncertainty on the trigger efficiency, as determined from the data, is 1.5%. An additional uncertainty comes from the limited Monte Carlo statistics.

The discrepancies of the results obtained with the PYTHIA and TWOGAM generators are considered as systematic uncertainties related to the Monte Carlo modelling. This difference is due to the calculated acceptance as well as to the unfolding procedure. An additional contribution to this modelling uncertainty is evaluated by repeating the analysis doubling or halving the VDM component of the TWOGAM generator and is found to be negligible.

4.3 Extraction of F_2^γ

The photon structure function F_2^γ/α is derived from the cross section of Equation 1 and the target-photon flux calculated by the program GALUGA [21] as:

$$F_2^\gamma(x, Q^2)/\alpha = \frac{\Delta\sigma_{\text{meas}}(\text{e}^+\text{e}^- \rightarrow \text{e}^+\text{e}^- \text{hadrons})}{\Delta\sigma_{\text{Galuga}}(\text{e}^+\text{e}^- \rightarrow \text{e}^+\text{e}^- \text{hadrons})}$$

The program calculates the theoretical value $\Delta\sigma_{\text{Galuga}}$ in the given Q^2 and x range setting $F_2^\gamma = 1$ and F_L^γ to the QPM value [22]. In practice the F_L^γ contribution to the cross section is smaller than 1%, due to the small value of y . The running of the fine-structure constant with Q^2 is included. A GVDM form factor is used in the calculation for the target photon virtuality whose average value is of the order of 0.07 GeV 2 . The low polar-angle calorimeter acceptance for the tagged and the anti-tagged electron and the $W_{\gamma\gamma} > 4$ GeV requirement are taken into account. The uncertainty on $\Delta\sigma_{\text{Galuga}}$, as estimated by comparing the GVDM to a ρ form factor, is 2%.

The contribution of radiative corrections to the cross section is evaluated by using the program RADCOR [23], which includes initial and final state radiation for the reaction $\text{e}^+\text{e}^- \rightarrow \text{e}^+\text{e}^- \mu^+ \mu^-$. The corrections are mainly due to initial state radiation from the electron scattered at large angle. Final state radiation is detected together with the scattered electron due to the finite granularity of the calorimeter. Initial state radiation from the electron producing the quasi-real target photon is very small. The calculations are performed at the generator level

using the Q^2 from the electron variables and $W_{\gamma\gamma}$ from the muon pair. The measured F_2^γ/α is multiplied by the ratio, \mathcal{R} , of the non-radiative and the total cross section, shown in Tables 6 and 7 for different values of x and Q^2 .

The F_2^γ values, averaged over the x intervals, are first obtained for each individual data set. The results are statistically compatible and, consequently, a weighted average of F_2^γ is calculated for the Q^2 ranges with average values 12.4 GeV^2 , 16.7 GeV^2 and 25.5 GeV^2 . This procedure is applied to data unfolded separately with PYTHIA and TWOGAM and the two different values are shown in Figure 5. Their average value is given in Table 6 and in Figure 6 for each x interval of expected average value $\langle x \rangle$. In addition to the systematic uncertainty on the cross section, presented in Table 5, two systematic uncertainties are further considered in the extraction of F_2^γ . The first uncertainty, of 2%, is associated to the GALUGA calculations. The second uncertainty, also of 2%, covers the estimation of the initial-state and final-state radiative corrections. The uncertainty on initial-state radiation is assessed by changing the angular and momentum criteria which separate soft from hard photons in the Monte Carlo programs. The uncertainty on final-state radiation is estimated by varying the cone angle of the calorimeter for which final state radiation is detected together with the scattered electron.

A comparison of the data with the existing parameterisations as obtained with the PDFLIB library [24] shows that our data are not well described by the leading-order parton density functions. In Figure 6 the data are compared with the predictions of the leading- and higher-order parton density functions GRV [25] and the higher-order parton density functions CJK [10]. The best agreement is found for the higher-order GRV [25] predictions. In all cases four quarks, u, d, s and c are used. The pure QPM prediction for $\gamma\gamma \rightarrow q\bar{q}$ is also indicated, as calculated by using GALUGA with a mass of 0.32 GeV for the u and d quarks, 0.5 GeV for the s quark and 1.4 GeV for the c quark. It is clearly insufficient to describe the data.

4.4 Q^2 -evolution of F_2^γ

The Q^2 -evolution of F_2^γ , is studied in four x bins, $x = 0.01 - 0.1$, $x = 0.1 - 0.2$, $x = 0.2 - 0.3$ and $x = 0.3 - 0.5$ and the results are given in Table 7. In Figure 7 the F_2^γ/α values are presented for the lowest x bin and for a combined bin $x = 0.1 - 0.5$, together with our previous results [6]. Corrections for radiative effects are applied. The new measurements at $11 \text{ GeV}^2 \leq Q^2 \leq 14 \text{ GeV}^2$, $14 \text{ GeV}^2 \leq Q^2 \leq 20 \text{ GeV}^2$ and $20 \text{ GeV}^2 \leq Q^2 \leq 34 \text{ GeV}^2$ are in good agreement with our previous results. The expected linear growth with $\ln Q^2$ is observed in both x intervals. The function $a + b \ln(Q^2 / \text{GeV}^2)$ is fitted to the data, taking into account the total uncertainty calculated from the quadratic sum of statistical and systematic uncertainties. The fit results are: $a = 0.141 \pm 0.007$ and $b = 0.060 \pm 0.005$ for $x = 0.01 - 0.1$ with a confidence level of 44% and $a = 0.05 \pm 0.11$ and $b = 0.13 \pm 0.04$ for $x = 0.1 - 0.5$ with a confidence level of 71%.

The predictions of the leading- and higher-order parton density functions GRV [25] and the higher-order parton density functions CJK [10] are also indicated in Figure 7. The evolution is different for the different models and the data are better described by the higher-order GRV model.

5 Conclusions

The photon structure function F_2^γ is measured at LEP with the L3 detector at centre-of-mass energies $189 \leq \sqrt{s} \leq 209 \text{ GeV}$ in the Q^2 range $11 \text{ GeV}^2 \leq Q^2 \leq 34 \text{ GeV}^2$ and the x range

$0.006 \leq x \leq 0.556$. The data are better reproduced by the higher-order parton density function of GRV than by other parton distribution functions determined from the low energy data.

Combining the present results with previous L3 measurements, the Q^2 evolution is studied from 1.5 GeV^2 to 120 GeV^2 in the low- x region, $0.01 \leq x \leq 0.1$, and from 12.4 GeV^2 to 225 GeV^2 in the higher- x region, $0.1 < x \leq 0.5$. The measurements at different centre-of-mass energies are consistent and the $\ln Q^2$ evolution of F_2^γ is clearly confirmed.

References

- [1] I.C. Brock *et al.*, Nucl. Instr. Meth. A **381** (1996) 236.
- [2] L3 Coll., B. Adeva *et al.*, Nucl. Instr. Meth. A **289** (1990) 35;
L3 Coll., O. Adriani *et al.*, Phys. Rep. **236** (1993) 1;
M. Chemarin *et al.*, Nucl. Instr. Meth. A **349** (1994) 345;
M. Acciarri *et al.*, Nucl. Instr. Meth. A **351** (1994) 300;
A. Adam *et al.*, Nucl. Instr. Meth. A **383** (1996) 342.
- [3] V.M. Budnev *et al.*, Phys. Rep. **15** (1974) 181.
- [4] C. Berger, W. Wagner, Phys. Rep. **146** (1987) 1.
- [5] R. Nisius, Phys. Rep. **332** (2000) 165.
- [6] L3 Coll., M. Acciarri *et al.*, Phys. Lett. B **436** (1998) 403;
L3 Coll., M. Acciarri *et al.*, Phys. Lett. B **447** (1999) 147;
L3 Coll., M. Acciarri *et al.*, Phys. Lett. B **483** (2000) 373.
- [7] ALEPH Coll., R. Barate *et al.*, Phys. Lett. B **458** (1999) 152;
ALEPH Coll., A. Heister *et al.*, Eur. Phys. J. **30** (2003) 145;
OPAL Coll., G. Abbiendi *et al.*, Eur. Phys. J. **18** (2000) 15;
OPAL Coll., G. Abbiendi *et al.*, Phys. Lett. B **533** (2002) 207.
- [8] M. Krawczyk, A. Zembrzuski and M. Staszek, Phys. Rep. **265** (2001) 165.
- [9] M. Klasen, Rev. Mod. Phys. **74** (2002) 1221.
- [10] F. Cornet *et al.*, Phys. Rev. D **68** (2003) 014010.
We thank Paweł Jankowski for providing us the CJK predictions for the photon structure function.
- [11] ALEPH, L3 and OPAL Coll., Eur. Phys. J. **23** (2002) 201.
- [12] PHOJET version 1.05c is used;
R. Engel, Z. Phys. C **66** (1995) 203;
R. Engel and J. Ranft, Phys. Rev. D **54** (1996) 4344.
- [13] PYTHIA version 6.203 is used;
T. Sjostrand *et al.*, Comp. Phys. Comm. **135** (2001) 238.
- [14] TWOGAM version 1.71 is used;
S. Nova, A. Olshevski, T. Todorov, DELPHI Note 90-35 (1990).
We thank our colleagues from DELPHI for having made their program available to us.

- [15] A. Capella *et al.*, Phys. Rep. **236** (1994) 225.
- [16] JETSET version 7.4 is used;
T. Sjostrand, Comp. Phys. Comm. **82** (1994) 74.
- [17] DIAG36 Monte Carlo;
F.A. Berends, P.H. Daverveldt and R. Kleiss, Nucl. Phys. B **253** (1985) 441;
F.A. Berends, P.H. Daverveldt and R. Kleiss, Comp. Phys. Comm. **40** (1986) 285.
- [18] GEANT version 3.15 is used;
R. Brun *et al.*, preprint CERN DD/EE/84-1 (1984), revised 1987.
- [19] H. Fesefeldt, RWTH Aachen report PITHA 85/2 (1985).
- [20] G. D'Agostini, Nucl. Instr. Meth. A **362** (1995) 487.
- [21] GALUGA version 2.0 is used;
G.A. Schuler, Comp. Phys. Comm. **108** (1998) 279.
The program GALUGA writes the cross section in term of σ_{TT} and σ_{TL} , these expressions have been modified by A. Finch in order to have the cross section in terms of F_2^γ and F_1^γ [4], we thank him for making his program available to us.
- [22] T.F. Walsh and P. Zerwas, Phys. Lett. B **44** (1973) 195;
R.L. Kingsley, Nucl. Phys. B **60** (1973) 45.
- [23] RADCOR Monte Carlo;
F.A. Berends, P.H. Daverveldt and R. Kleiss, Nucl. Phys. B **253** (1985) 421;
F.A. Berends, P.H. Daverveldt and R. Kleiss, Comp. Phys. Comm. **40** (1986) 271.
- [24] H. Plothow-Besch, Comp. Phys. Comm. **75** (1993) 396.
- [25] M. Glück, E. Reya and A. Vogt, Phys. Rev. D **45** (1992) 3986;
M. Glück, E. Reya and A. Vogt, Phys. Rev. D **46** (1992) 1973.
The values given in appendix A2 (pg. 1977) are used.

The L3 Collaboration:

P.Achard,²⁰ O.Adriani,¹⁷ M.Aguilar-Benitez,²⁵ J.Alcaraz,²⁵ G.Alemanni,²³ J.Allaby,¹⁸ A.Aloisio,²⁹ M.G.Alvaggi,²⁹ H.Anderhub,⁴⁹ V.P.Andreev,^{6,34} F.Anselmo,⁸ A.Areftev,²⁸ T.Azemoon,³ T.Aziz,⁹ P.Bagnaia,³⁹ A.Bajo,²⁵ G.Baksay,²⁶ L.Baksay,²⁶ S.V.Baldew,² S.Banerjee,⁹ Sw.Banerjee,⁴ A.Barczyk,^{49,47} R.Barillère,¹⁸ P.Bartalini,²³ M.Basile,⁸ N.Batalova,⁴⁶ R.Battiston,³³ A.Bay,²³ F.Becattini,¹⁷ U.Becker,¹³ F.Behner,⁴⁹ L.Bellucci,¹⁷ R.Berbeco,³ J.Berdugo,²⁵ P.Berges,¹³ B.Bertucci,³³ B.L.Betev,⁴⁹ M.Biasini,³³ M.Biglietti,²⁹ A.Biland,⁴⁹ J.J.Blaising,⁴ S.C.Blyth,³⁵ G.J.Bobbink,² A.Böhm,¹ L.Boldizsar,¹² B.Borgia,³⁹ S.Bottai,¹⁷ D.Bourilkov,⁴⁹ M.Bourquin,²⁰ S.Braccini,²⁰ J.G.Branson,⁴¹ F.Brochu,⁴ J.D.Burger,¹³ W.J.Burger,³³ X.D.Cai,¹³ M.Capell,¹³ G.Cara Romeo,⁸ G.Carlini,²⁹ A.Cartacci,¹⁷ J.Casaus,²⁵ F.Cavallari,³⁹ N.Cavallo,³⁶ C.Cecchi,³³ M.Cerrada,²⁵ M.Chamizo,²⁰ Y.H.Chang,⁴⁴ M.Chemarin,²⁴ A.Chen,⁴⁴ G.Chen,⁷ G.M.Chen,⁷ H.F.Chen,²² H.S.Chen,⁷ G.Chiefari,²⁹ L.Cifarelli,⁴⁰ F.Cindolo,⁸ I.Clare,¹³ R.Clare,³⁸ G.Coignet,⁴ N.Colino,²⁵ S.Costantini,³⁹ B.de la Cruz,²⁵ S.Cucciarelli,³³ R.de Asmundis,²⁹ P.Déglon,²⁰ J.Debreczeni,¹² A.Degré,⁴ K.Dehmelt,²⁶ K.Deiters,⁴⁷ D.della Volpe,²⁹ E.Delmeire,²⁰ P.Denes,³⁷ F.DeNotaristefani,³⁹ A.De Salvo,⁴⁹ M.Diemoz,³⁹ M.Dierckxsens,² C.Dionisi,³⁹ M.Dittmar,⁴⁹ A.Doria,²⁹ M.T.Dova,^{10,‡} D.Duchesneau,⁴ M.Duda,¹ B.Echenard,²⁰ A.Eline,¹⁸ A.El Hage,¹ H.El Mamouni,²⁴ A.Engler,³⁵ F.J.Eppling,¹³ P.Extermann,²⁰ M.A.Falagan,²⁵ S.Falciano,³⁹ A.Favara,³² J.Fay,²⁴ O.Fedin,³⁴ M.Felcini,⁴⁹ T.Ferguson,³⁵ H.Fesefeldt,¹ E.Fiandrini,³³ J.H.Field,²⁰ F.Filthaut,³¹ P.H.Fisher,¹³ W.Fisher,³⁷ I.Fisk,⁴¹ G.Forconi,¹³ K.Freudenreich,⁴⁹ C.Furetta,²⁷ Yu.Galaktionov,^{28,13} S.N.Ganguli,⁹ P.Garcia-Abia,²⁵ M.Gataullin,³² S.Gentile,³⁹ S.Giagu,³⁹ Z.F.Gong,²² G.Grenier,²⁴ O.Grimm,⁴⁹ M.W.Gruenewald,¹⁶ M.Guida,⁴⁰ V.K.Gupta,³⁷ A.Gurtu,⁹ L.J.Gutay,⁴⁶ D.Haas,⁵ D.Hatzifotiadou,⁸ T.Hebbeker,¹ A.Hervé,¹⁸ J.Hirschfelder,³⁵ H.Hofer,⁴⁹ M.Hohlmann,²⁶ G.Holzner,⁴⁹ S.R.Hou,⁴⁴ B.N.Jin,⁷ P.Jindal,¹⁴ L.W.Jones,³ P.de Jong,² I.Josa-Mutuberría,²⁵ M.Kaur,¹⁴ M.N.Kienzle-Focacci,²⁰ J.K.Kim,⁴³ J.Kirkby,¹⁸ W.Kittel,³¹ A.Klimentov,^{13,28} A.C.König,³¹ M.Kopal,⁴⁶ V.Koutsenko,^{13,28} M.Kräber,⁴⁹ R.W.Kraemer,³⁵ A.Krüger,⁴⁸ A.Kunin,¹³ P.Ladron de Guevara,²⁵ I.Laktineh,²⁴ G.Landi,¹⁷ M.Lebeau,¹⁸ A.Lebedev,¹³ P.Lebrun,²⁴ P.Lecomte,⁴⁹ P.Lecoq,¹⁸ P.Le Coultre,⁴⁹ J.M.Le Goff,¹⁸ R.Leiste,⁴⁸ M.Levtchenko,²⁷ P.Levtchenko,³⁴ C.Li,²² S.Likhoded,⁴⁸ C.H.Lin,⁴⁴ W.T.Lin,⁴⁴ F.L.Linde,² L.Lista,²⁹ Z.A.Liu,⁷ W.Lohmann,⁴⁸ E.Longo,³⁹ Y.S.Lu,⁷ C.Luci,³⁹ L.Luminari,³⁹ W.Lustermann,⁴⁹ W.G.Ma,²² L.Malgeri,¹⁸ A.Malinin,²⁸ C.Maña,²⁵ J.Mans,³⁷ J.P.Martin,²⁴ F.Marzano,³⁹ K.Mazumdar,⁹ R.R.McNeil,⁶ S.Melegi,^{18,29} P.Mermod,²⁰ L.Merola,²⁹ M.Meschini,¹⁷ W.J.Metzger,³¹ A.Mihul,¹¹ H.Milcent,¹⁸ G.Mirabelli,³⁹ J.Mnich,¹ G.B.Mohanty,⁹ G.S.Muanza,²⁴ A.J.M.Muijs,² B.Musicar,⁴¹ M.Musy,³⁹ S.Nagy,¹⁵ S.Natale,²⁰ M.Napolitano,²⁹ F.Nessi-Tedaldi,⁴⁹ H.Newman,³² A.Nisati,³⁹ T.Novak,³¹ H.Nowak,⁴⁸ R.Ofierzynski,⁴⁹ G.Organtini,³⁹ I.Pal,⁴⁶ C.Palomares,²⁵ P.Paolucci,²⁹ R.Paramatti,³⁹ G.Passaleva,¹⁷ S.Patricelli,²⁹ T.Paul,¹⁰ M.Pauluzzi,³³ C.Paus,¹³ F.Pauss,⁴⁹ M.Pedace,³⁹ S.Pensotti,²⁷ D.Perret-Gallix,⁴ D.Piccolo,²⁹ F.Pierella,⁸ M.Pioppi,³³ P.A.Piroué,³⁷ E.Pistolesi,²⁷ V.Plyaskin,²⁸ M.Pohl,²⁰ V.Pojidaev,¹⁷ J.Pothier,¹⁸ D.Prokofiev,³⁴ G.Rahal-Callot,⁴⁹ M.A.Rahaman,⁹ P.Raics,¹⁵ N.Raja,⁹ R.Ramelli,⁴⁹ P.G.Rancoita,²⁷ R.Ranieri,¹⁷ A.Raspereza,⁴⁸ P.Razis,³⁰ D.Ren,⁴⁹ M.Rescigno,³⁹ S.Reucroft,¹⁰ S.Riemann,⁴⁸ K.Riles,³ B.P.Roe,³ L.Romero,²⁵ A.Rosca,⁴⁸ C.Rosemann,¹ C.Rosenbleck,¹ S.Rosier-Lees,⁴ S.Roth,¹ J.A.Rubio,¹⁸ G.Ruggiero,¹⁷ H.Rykaczewski,⁴⁹ A.Sakharov,⁴⁹ S.Saremi,⁶ S.Sarkar,³⁹ J.Salicio,¹⁸ E.Sánchez,²⁵ C.Schäfer,¹⁸ V.Schegelsky,³⁴ H.Schopper,²¹ D.J.Schotanus,³¹ C.Sciacca,²⁹ L.Servoli,³³ S.Shevchenko,³² N.Shivarov,⁴² V.Shoutko,¹³ E.Shumilov,²⁸ A.Shvorob,³² D.Son,⁴³ C.Souga,²⁴ P.Spillantini,¹⁷ M.Steuer,¹³ D.P.Stickland,³⁷ B.Stoyanov,⁴² A.Straessner,²⁰ K.Sudhakar,⁹ G.Sultanov,⁴² L.Z.Sun,²² S.Sushkov,¹ H.Suter,⁴⁹ J.D.Swain,¹⁰ Z.Szillasi,^{26,¶} X.W.Tang,⁷ P.Tarjan,¹⁵ L.Tauscher,⁵ L.Taylor,¹⁰ B.Tellili,²⁴ D.Teyssier,²⁴ C.Timmermans,³¹ Samuel C.C.Ting,¹³ S.M.Ting,¹³ S.C.Tonwar,⁹ J.Tóth,¹² C.Tully,³⁷ K.L.Tung,⁷ J.Ulbricht,⁴⁹ E.Valente,³⁹ R.T.Van de Walle,³¹ R.Vasquez,⁴⁶ V.Veszpremi,²⁶ G.Vesztergombi,¹² I.Vetlitsky,²⁸ G.Viertel,⁴⁹ S.Villa,³⁸ M.Vivargent,⁴ S.Vlachos,⁵ I.Vodopianov,²⁶ H.Vogel,³⁵ H.Vogt,⁴⁸ I.Vorobiev,^{35,28} A.A.Vorobyov,³⁴ M.Wadhwa,⁵ Q.Wang,³¹ X.L.Wang,²² Z.M.Wang,²² M.Weber,¹⁸ S.Wynhoff,³⁷ L.Xia,³² Z.Z.Xu,²² J.Yamamoto,³ B.Z.Yang,²² C.G.Yang,⁷ H.J.Yang,³ M.Yang,⁷ S.C.Yeh,⁴⁵ An.Zalite,³⁴ Yu.Zalite,³⁴ Z.P.Zhang,²² J.Zhao,²² G.Y.Zhu,⁷ R.Y.Zhu,³² H.L.Zhuang,⁷ A.Zichichi,^{8,18,19} B.Zimmermann,⁴⁹ M.Zöller,¹

- 1 III. Physikalisches Institut, RWTH, D-52056 Aachen, Germany[§]
 2 National Institute for High Energy Physics, NIKHEF, and University of Amsterdam, NL-1009 DB Amsterdam,
 The Netherlands
 3 University of Michigan, Ann Arbor, MI 48109, USA
 4 Laboratoire d'Annecy-le-Vieux de Physique des Particules, LAPP,IN2P3-CNRS, BP 110, F-74941
 Annecy-le-Vieux CEDEX, France
 5 Institute of Physics, University of Basel, CH-4056 Basel, Switzerland
 6 Louisiana State University, Baton Rouge, LA 70803, USA
 7 Institute of High Energy Physics, IHEP, 100039 Beijing, China[△]
 8 University of Bologna and INFN-Sezione di Bologna, I-40126 Bologna, Italy
 9 Tata Institute of Fundamental Research, Mumbai (Bombay) 400 005, India
 10 Northeastern University, Boston, MA 02115, USA
 11 Institute of Atomic Physics and University of Bucharest, R-76900 Bucharest, Romania
 12 Central Research Institute for Physics of the Hungarian Academy of Sciences, H-1525 Budapest 114, Hungary[‡]
 13 Massachusetts Institute of Technology, Cambridge, MA 02139, USA
 14 Panjab University, Chandigarh 160 014, India
 15 KLTE-ATOMKI, H-4010 Debrecen, Hungary[¶]
 16 Department of Experimental Physics, University College Dublin, Belfield, Dublin 4, Ireland
 17 INFN Sezione di Firenze and University of Florence, I-50125 Florence, Italy
 18 European Laboratory for Particle Physics, CERN, CH-1211 Geneva 23, Switzerland
 19 World Laboratory, FBLJA Project, CH-1211 Geneva 23, Switzerland
 20 University of Geneva, CH-1211 Geneva 4, Switzerland
 21 University of Hamburg, D-22761 Hamburg, Germany
 22 Chinese University of Science and Technology, USTC, Hefei, Anhui 230 029, China[△]
 23 University of Lausanne, CH-1015 Lausanne, Switzerland
 24 Institut de Physique Nucléaire de Lyon, IN2P3-CNRS, Université Claude Bernard, F-69622 Villeurbanne, France
 25 Centro de Investigaciones Energéticas, Medioambientales y Tecnológicas, CIEMAT, E-28040 Madrid, Spain[♭]
 26 Florida Institute of Technology, Melbourne, FL 32901, USA
 27 INFN-Sezione di Milano, I-20133 Milan, Italy
 28 Institute of Theoretical and Experimental Physics, ITEP, Moscow, Russia
 29 INFN-Sezione di Napoli and University of Naples, I-80125 Naples, Italy
 30 Department of Physics, University of Cyprus, Nicosia, Cyprus
 31 Radboud University and NIKHEF, NL-6525 ED Nijmegen, The Netherlands
 32 California Institute of Technology, Pasadena, CA 91125, USA
 33 INFN-Sezione di Perugia and Università Degli Studi di Perugia, I-06100 Perugia, Italy
 34 Nuclear Physics Institute, St. Petersburg, Russia
 35 Carnegie Mellon University, Pittsburgh, PA 15213, USA
 36 INFN-Sezione di Napoli and University of Potenza, I-85100 Potenza, Italy
 37 Princeton University, Princeton, NJ 08544, USA
 38 University of California, Riverside, CA 92521, USA
 39 INFN-Sezione di Roma and University of Rome, “La Sapienza”, I-00185 Rome, Italy
 40 University and INFN, Salerno, I-84100 Salerno, Italy
 41 University of California, San Diego, CA 92093, USA
 42 Bulgarian Academy of Sciences, Central Lab. of Mechatronics and Instrumentation, BU-1113 Sofia, Bulgaria
 43 The Center for High Energy Physics, Kyungpook National University, 702-701 Taegu, Republic of Korea
 44 National Central University, Chung-Li, Taiwan, China
 45 Department of Physics, National Tsing Hua University, Taiwan, China
 46 Purdue University, West Lafayette, IN 47907, USA
 47 Paul Scherrer Institut, PSI, CH-5232 Villigen, Switzerland
 48 DESY, D-15738 Zeuthen, Germany
 49 Eidgenössische Technische Hochschule, ETH Zürich, CH-8093 Zürich, Switzerland
 § Supported by the German Bundesministerium für Bildung, Wissenschaft, Forschung und Technologie.
 ‡ Supported by the Hungarian OTKA fund under contract numbers T019181, F023259 and T037350.
 ¶ Also supported by the Hungarian OTKA fund under contract number T026178.
 ♭ Supported also by the Comisión Interministerial de Ciencia y Tecnología.
 ♯ Also supported by CONICET and Universidad Nacional de La Plata, CC 67, 1900 La Plata, Argentina.
 △ Supported by the National Natural Science Foundation of China.

$\langle \sqrt{s} \rangle$ (GeV)	\mathcal{L} (pb $^{-1}$)	Events	$e^+e^- \rightarrow e^+e^-\tau^+\tau^-$	$e^+e^- \rightarrow q\bar{q}(\gamma)$	Purity (%)
$Q^2 = 11 - 14 \text{ GeV}^2$					
189	171.8	1884	107.6	5.7	94
194	111.4	1197	76.3	3.3	93
200	109.3	1187	74.9	3.7	93
206	215.6	2418	129.6	7.7	94
$Q^2 = 14 - 20 \text{ GeV}^2$					
189	171.8	2046	128.6	9.7	93
194	111.4	1347	91.2	5.4	93
200	109.3	1359	89.5	4.9	93
206	215.6	2886	177.4	8.7	94
$Q^2 = 20 - 34 \text{ GeV}^2$					
189	171.8	1922	143.9	8.1	92
194	111.4	1331	103.6	5.8	92
200	109.3	1287	101.6	6.7	92
206	215.6	2859	202.5	12.7	92

Table 1: The average e^+e^- centre-of-mass energies, $\langle \sqrt{s} \rangle$, and the corresponding luminosities for the four data samples together with the number of selected events in the Q^2 intervals $11 \text{ GeV}^2 \leq Q^2 \leq 14 \text{ GeV}^2$, $14 \text{ GeV}^2 \leq Q^2 \leq 20 \text{ GeV}^2$ and $20 \text{ GeV}^2 \leq Q^2 \leq 34 \text{ GeV}^2$. The numbers of expected background events from the $e^+e^- \rightarrow e^+e^-\tau^+\tau^-$ and $e^+e^- \rightarrow q\bar{q}(\gamma)$ processes and the signal purity are also listed.

$\langle \sqrt{s} \rangle$		189 GeV	194 GeV	200 GeV	206 GeV
$Q^2 = 11 - 14 \text{ GeV}^2$					
Δx range	$\langle x \rangle$	$\Delta\sigma/\Delta x$ (pb)	$\Delta\sigma/\Delta x$ (pb)	$\Delta\sigma/\Delta x$ (pb)	$\Delta\sigma/\Delta x$ (pb)
0.006 – 0.023	0.013	$103.6 \pm 8.5 \pm 14.5$	$108.2 \pm 10.8 \pm 15.4$	$106.4 \pm 10.2 \pm 10.4$	$115.3 \pm 7.8 \pm 16.4$
0.023 – 0.040	0.031	$63.4 \pm 5.3 \pm 4.3$	$67.0 \pm 6.5 \pm 8.4$	$63.9 \pm 6.3 \pm 5.2$	$69.6 \pm 4.5 \pm 7.7$
0.040 – 0.060	0.050	$52.0 \pm 4.0 \pm 2.9$	$55.7 \pm 5.1 \pm 7.8$	$53.4 \pm 5.5 \pm 5.3$	$52.0 \pm 3.6 \pm 5.4$
0.060 – 0.090	0.075	$45.0 \pm 3.4 \pm 2.2$	$47.7 \pm 4.4 \pm 6.1$	$44.0 \pm 4.0 \pm 4.4$	$43.8 \pm 2.8 \pm 5.3$
0.090 – 0.120	0.10	$40.2 \pm 2.9 \pm 1.8$	$40.8 \pm 3.9 \pm 5.3$	$39.3 \pm 3.6 \pm 4.3$	$39.6 \pm 2.8 \pm 5.1$
0.120 – 0.160	0.14	$37.9 \pm 2.8 \pm 2.3$	$37.4 \pm 3.4 \pm 5.3$	$36.9 \pm 3.4 \pm 4.2$	$37.9 \pm 2.5 \pm 4.4$
0.160 – 0.205	0.18	$34.8 \pm 2.5 \pm 1.3$	$33.9 \pm 2.9 \pm 4.7$	$33.0 \pm 2.9 \pm 4.3$	$35.8 \pm 2.4 \pm 4.3$
0.205 – 0.260	0.23	$33.3 \pm 2.4 \pm 1.3$	$31.9 \pm 3.1 \pm 4.8$	$31.6 \pm 2.8 \pm 4.0$	$32.6 \pm 2.0 \pm 4.4$
0.260 – 0.330	0.29	$29.8 \pm 2.1 \pm 1.7$	$29.1 \pm 2.9 \pm 4.0$	$28.3 \pm 2.7 \pm 3.7$	$30.7 \pm 1.9 \pm 4.4$
0.330 – 0.400	0.36	$29.9 \pm 2.1 \pm 1.3$	$27.5 \pm 2.7 \pm 4.0$	$25.5 \pm 2.6 \pm 3.8$	$29.5 \pm 1.8 \pm 3.9$
$Q^2 = 14 - 20 \text{ GeV}^2$					
0.006 – 0.023	0.013	$97.0 \pm 8.5 \pm 12.7$	$100.4 \pm 10.2 \pm 9.8$	$102.4 \pm 10.4 \pm 11.1$	$113.0 \pm 7.7 \pm 11.5$
0.023 – 0.040	0.031	$59.3 \pm 4.9 \pm 3.6$	$64.0 \pm 6.5 \pm 4.9$	$64.2 \pm 7.1 \pm 6.2$	$72.2 \pm 5.2 \pm 7.8$
0.040 – 0.060	0.050	$49.6 \pm 4.3 \pm 5.7$	$50.8 \pm 5.2 \pm 5.0$	$53.4 \pm 5.3 \pm 4.3$	$55.8 \pm 3.6 \pm 2.7$
0.060 – 0.090	0.075	$40.8 \pm 2.9 \pm 1.7$	$42.5 \pm 3.9 \pm 1.9$	$44.5 \pm 4.2 \pm 2.6$	$47.8 \pm 2.9 \pm 3.1$
0.090 – 0.120	0.10	$36.1 \pm 2.9 \pm 1.9$	$38.0 \pm 3.6 \pm 2.3$	$37.9 \pm 3.6 \pm 3.2$	$41.5 \pm 2.4 \pm 2.0$
0.120 – 0.160	0.14	$32.5 \pm 2.2 \pm 1.5$	$35.7 \pm 3.0 \pm 1.6$	$36.7 \pm 3.3 \pm 2.1$	$37.7 \pm 2.3 \pm 1.7$
0.160 – 0.205	0.18	$31.8 \pm 2.3 \pm 1.3$	$31.9 \pm 2.7 \pm 1.7$	$33.3 \pm 3.0 \pm 1.7$	$34.7 \pm 2.2 \pm 1.5$
0.205 – 0.260	0.23	$30.8 \pm 2.1 \pm 1.0$	$30.6 \pm 2.8 \pm 1.3$	$32.2 \pm 2.8 \pm 1.8$	$34.4 \pm 2.0 \pm 1.5$
0.260 – 0.330	0.29	$27.7 \pm 2.0 \pm 1.0$	$27.6 \pm 2.3 \pm 1.2$	$30.0 \pm 2.3 \pm 1.7$	$31.2 \pm 1.9 \pm 1.2$
0.330 – 0.400	0.36	$28.1 \pm 2.1 \pm 1.1$	$26.8 \pm 2.4 \pm 1.3$	$29.4 \pm 2.8 \pm 1.3$	$29.0 \pm 1.9 \pm 1.0$
0.400 – 0.467	0.42	$26.7 \pm 2.1 \pm 2.1$	$25.2 \pm 2.5 \pm 1.8$	$26.8 \pm 2.7 \pm 1.7$	$27.8 \pm 1.9 \pm 1.1$
$Q^2 = 20 - 34 \text{ GeV}^2$					
0.023 – 0.040	0.031	$48.6 \pm 5.4 \pm 3.6$	$54.3 \pm 6.5 \pm 3.3$	$37.4 \pm 3.6 \pm 2.4$	$39.5 \pm 2.6 \pm 2.0$
0.040 – 0.060	0.050	$41.9 \pm 4.1 \pm 4.1$	$36.0 \pm 3.4 \pm 2.4$	$37.4 \pm 3.6 \pm 2.4$	$39.5 \pm 2.6 \pm 2.0$
0.060 – 0.090	0.075	$35.8 \pm 2.8 \pm 1.7$	$36.0 \pm 3.4 \pm 2.4$	$37.4 \pm 3.6 \pm 2.4$	$39.5 \pm 2.6 \pm 2.0$
0.090 – 0.120	0.10	$32.8 \pm 2.7 \pm 2.2$	$32.1 \pm 3.3 \pm 1.4$	$32.4 \pm 3.3 \pm 1.9$	$36.3 \pm 2.6 \pm 1.3$
0.120 – 0.160	0.14	$29.1 \pm 2.5 \pm 1.7$	$30.6 \pm 2.8 \pm 2.4$	$32.1 \pm 3.0 \pm 2.5$	$33.6 \pm 2.2 \pm 1.2$
0.160 – 0.205	0.18	$27.7 \pm 2.1 \pm 1.1$	$28.1 \pm 2.6 \pm 1.1$	$28.6 \pm 2.6 \pm 1.7$	$32.2 \pm 2.0 \pm 1.2$
0.205 – 0.260	0.23	$25.0 \pm 1.7 \pm 1.0$	$24.2 \pm 2.0 \pm 1.0$	$25.0 \pm 2.2 \pm 1.3$	$27.4 \pm 1.6 \pm 1.2$
0.260 – 0.330	0.29	$25.0 \pm 1.7 \pm 1.0$	$24.2 \pm 2.0 \pm 1.0$	$25.0 \pm 2.2 \pm 1.3$	$27.4 \pm 1.6 \pm 1.2$
0.330 – 0.400	0.36	$24.5 \pm 1.8 \pm 1.2$	$23.3 \pm 2.2 \pm 1.0$	$24.3 \pm 2.2 \pm 1.4$	$25.6 \pm 1.6 \pm 0.9$
0.400 – 0.467	0.42	$23.6 \pm 1.8 \pm 1.5$	$22.4 \pm 2.0 \pm 1.1$	$23.5 \pm 2.4 \pm 1.2$	$24.5 \pm 1.7 \pm 1.0$
0.467 – 0.556	0.49	$22.8 \pm 1.6 \pm 2.5$	$22.4 \pm 2.1 \pm 2.9$	$24.0 \pm 2.3 \pm 2.3$	$24.5 \pm 1.5 \pm 1.5$

Table 2: Cross sections $\Delta\sigma/\Delta x$ as a function of x for the reaction $e^+e^- \rightarrow e^+e^- \text{hadrons}$ for the four average values of \sqrt{s} , in three Q^2 intervals. The first uncertainty is statistical, the second systematic.

	$Q^2 = 11 - 14 \text{ GeV}^2$									
x range	0.006 — 0.023	0.023 — 0.040	0.040 — 0.060	0.060 — 0.090	0.090 — 0.120	0.120 — 0.160	0.160 — 0.205	0.205 — 0.260	0.260 — 0.330	0.330 — 0.400
0.006 – 0.023	1.00									
0.023 – 0.040	0.92	1.00								
0.040 – 0.060	0.75	0.92	1.00							
0.060 – 0.090	0.55	0.79	0.96	1.00						
0.090 – 0.120	0.45	0.67	0.85	0.94	1.00					
0.120 – 0.160	0.39	0.62	0.78	0.89	0.98	1.00				
0.160 – 0.205	0.28	0.50	0.67	0.80	0.95	0.97	1.00			
0.205 – 0.260	0.25	0.45	0.59	0.69	0.84	0.87	0.94	1.00		
0.260 – 0.330	0.22	0.38	0.49	0.59	0.79	0.82	0.91	0.99	1.00	
0.330 – 0.400	0.17	0.36	0.50	0.60	0.77	0.78	0.86	0.98	0.97	1.00

	$Q^2 = 14 - 20 \text{ GeV}^2$									
x range	0.006 — 0.023	0.023 — 0.040	0.040 — 0.060	0.060 — 0.090	0.090 — 0.120	0.120 — 0.160	0.160 — 0.205	0.205 — 0.260	0.260 — 0.330	0.330 — 0.400
0.006 – 0.023	1.00									
0.023 – 0.040	0.87	1.00								
0.040 – 0.060	0.74	0.95	1.00							
0.060 – 0.090	0.55	0.82	0.93	1.00						
0.090 – 0.120	0.54	0.79	0.89	0.98	1.00					
0.120 – 0.160	0.36	0.63	0.73	0.89	0.93	1.00				
0.160 – 0.205	0.31	0.60	0.71	0.85	0.89	0.98	1.00			
0.205 – 0.260	0.24	0.49	0.59	0.75	0.81	0.95	0.95	1.00		
0.260 – 0.330	0.18	0.40	0.50	0.64	0.71	0.87	0.88	0.97	1.00	
0.330 – 0.400	0.21	0.40	0.47	0.56	0.65	0.79	0.79	0.91	0.97	1.00
0.400 – 0.467	0.11	0.31	0.37	0.47	0.55	0.71	0.71	0.84	0.91	0.96

	$Q^2 = 20 - 34 \text{ GeV}^2$									
x range	0.023 — 0.040	0.040 — 0.060	0.060 — 0.090	0.090 — 0.120	0.120 — 0.160	0.160 — 0.205	0.205 — 0.260	0.260 — 0.330	0.330 — 0.400	0.400 — 0.467
0.023 – 0.040	1.00									
0.040 – 0.060	0.92	1.00								
0.060 – 0.090	0.87	0.96	1.00							
0.090 – 0.120	0.80	0.88	0.97	1.00						
0.120 – 0.160	0.66	0.75	0.89	0.96	1.00					
0.160 – 0.205	0.62	0.71	0.82	0.91	0.97	1.00				
0.205 – 0.260	0.58	0.64	0.76	0.86	0.93	0.98	1.00			
0.260 – 0.330	0.47	0.54	0.66	0.77	0.88	0.95	0.97	1.00		
0.330 – 0.400	0.43	0.49	0.61	0.71	0.81	0.88	0.92	0.97	1.00	
0.400 – 0.467	0.38	0.45	0.55	0.63	0.73	0.78	0.83	0.91	0.98	1.00
0.467 – 0.556	0.39	0.44	0.54	0.63	0.73	0.78	0.84	0.91	0.98	1.00

Table 3: Correlation matrices obtained with the PYTHIA Monte Carlo for the data at $\sqrt{s} = 189 \text{ GeV}$ for the three Q^2 intervals.

	$Q^2 = 11 - 14 \text{ GeV}^2$									
x range	0.006 — 0.023	0.023 — 0.040	0.040 — 0.060	0.060 — 0.090	0.090 — 0.120	0.120 — 0.160	0.160 — 0.205	0.205 — 0.260	0.260 — 0.330	0.330 — 0.400
0.006–0.023	1.00									
0.023–0.040	0.91	1.00								
0.040–0.060	0.79	0.96	1.00							
0.060–0.090	0.63	0.86	0.95	1.00						
0.090–0.120	0.52	0.74	0.86	0.95	1.00					
0.120–0.160	0.46	0.66	0.78	0.90	0.98	1.00				
0.160–0.205	0.36	0.57	0.69	0.82	0.92	0.97	1.00			
0.205–0.260	0.27	0.45	0.56	0.69	0.80	0.88	0.97	1.00		
0.260–0.330	0.24	0.42	0.52	0.65	0.73	0.83	0.93	0.98	1.00	
0.330–0.400	0.19	0.36	0.45	0.58	0.64	0.74	0.86	0.93	0.98	1.00

	$Q^2 = 14 - 20 \text{ GeV}^2$									
x range	0.006 — 0.023	0.023 — 0.040	0.040 — 0.060	0.060 — 0.090	0.090 — 0.120	0.120 — 0.160	0.160 — 0.205	0.205 — 0.260	0.260 — 0.330	0.330 — 0.400
0.006–0.023	1.00									
0.023–0.040	0.90	1.00								
0.040–0.060	0.76	0.95	1.00							
0.060–0.090	0.62	0.86	0.96	1.00						
0.090–0.120	0.50	0.74	0.87	0.96	1.00					
0.120–0.160	0.43	0.66	0.78	0.90	0.97	1.00				
0.160–0.205	0.36	0.56	0.68	0.81	0.90	0.96	1.00			
0.205–0.260	0.29	0.45	0.57	0.70	0.78	0.87	0.96	1.00		
0.260–0.330	0.23	0.38	0.49	0.60	0.68	0.77	0.90	0.97	1.00	
0.330–0.400	0.17	0.32	0.43	0.56	0.63	0.73	0.85	0.95	0.98	1.00
0.400–0.467	0.16	0.28	0.38	0.48	0.55	0.64	0.77	0.88	0.95	0.98

	$Q^2 = 20 - 34 \text{ GeV}^2$									
x range	0.023 — 0.040	0.040 — 0.060	0.060 — 0.090	0.090 — 0.120	0.120 — 0.160	0.160 — 0.205	0.205 — 0.260	0.260 — 0.330	0.330 — 0.400	0.400 — 0.467
0.023–0.040	1.00									
0.040–0.060	0.92	1.00								
0.060–0.090	0.85	0.95	1.00							
0.090–0.120	0.73	0.87	0.96	1.00						
0.120–0.160	0.62	0.77	0.88	0.96	1.00					
0.160–0.205	0.52	0.66	0.78	0.88	0.96	1.00				
0.205–0.260	0.45	0.61	0.71	0.81	0.91	0.98	1.00			
0.260–0.330	0.35	0.50	0.59	0.69	0.79	0.90	0.96	1.00		
0.330–0.400	0.34	0.45	0.54	0.62	0.69	0.78	0.85	0.93	1.00	
0.400–0.467	0.25	0.37	0.46	0.56	0.66	0.78	0.87	0.96	0.98	1.00
0.467–0.556	0.25	0.36	0.44	0.52	0.61	0.72	0.81	0.90	0.97	0.98

Table 4: Correlation matrices obtained with the TWOGAM Monte Carlo for the data at $\sqrt{s} = 189 \text{ GeV}$ for the three Q^2 intervals.

Source of systematic uncertainties	Uncertainty in %
Tagging calorimeter polar angle	0.9 – 8.0
Tagging calorimeter energy	1.6 – 2.5
Anti-tag energy	0.4
Number of particles	0.2 – 2.6
Total energy in the calorimeters	0.2
Trigger efficiency	1.5
Monte Carlo statistics	0.2 – 0.5
Model dependence	0.7 – 9.9

Table 5: Systematic uncertainties on the measured cross sections.

x range	$\langle x \rangle$	\mathcal{R}	F_2^γ/α
$Q^2 = 11 - 14 \text{ GeV}^2$			
0.006 – 0.023	0.013	0.92	$0.302 \pm 0.013 \pm 0.026 \pm 0.029$
0.023 – 0.040	0.031	0.90	$0.245 \pm 0.011 \pm 0.021 \pm 0.010$
0.040 – 0.060	0.050	0.88	$0.257 \pm 0.011 \pm 0.023 \pm 0.012$
0.060 – 0.090	0.075	0.90	$0.296 \pm 0.012 \pm 0.028 \pm 0.009$
0.090 – 0.120	0.10	0.89	$0.315 \pm 0.013 \pm 0.032 \pm 0.007$
0.120 – 0.160	0.14	0.90	$0.365 \pm 0.015 \pm 0.038 \pm 0.008$
0.160 – 0.205	0.18	0.88	$0.399 \pm 0.017 \pm 0.043 \pm 0.007$
0.205 – 0.260	0.23	0.89	$0.441 \pm 0.018 \pm 0.049 \pm 0.011$
0.260 – 0.330	0.29	0.88	$0.483 \pm 0.020 \pm 0.054 \pm 0.013$
0.330 – 0.400	0.36	0.89	$0.536 \pm 0.023 \pm 0.059 \pm 0.025$
$Q^2 = 14 - 20 \text{ GeV}^2$			
0.006 – 0.023	0.013	0.93	$0.310 \pm 0.014 \pm 0.020 \pm 0.028$
0.023 – 0.040	0.031	0.88	$0.258 \pm 0.012 \pm 0.014 \pm 0.018$
0.040 – 0.060	0.050	0.90	$0.275 \pm 0.012 \pm 0.014 \pm 0.017$
0.060 – 0.090	0.075	0.90	$0.288 \pm 0.011 \pm 0.014 \pm 0.008$
0.090 – 0.120	0.10	0.89	$0.316 \pm 0.013 \pm 0.015 \pm 0.014$
0.120 – 0.160	0.14	0.90	$0.337 \pm 0.013 \pm 0.016 \pm 0.007$
0.160 – 0.205	0.18	0.89	$0.381 \pm 0.015 \pm 0.018 \pm 0.006$
0.205 – 0.260	0.23	0.88	$0.424 \pm 0.017 \pm 0.019 \pm 0.008$
0.260 – 0.330	0.29	0.88	$0.471 \pm 0.018 \pm 0.020 \pm 0.009$
0.330 – 0.400	0.36	0.87	$0.510 \pm 0.021 \pm 0.022 \pm 0.007$
0.400 – 0.467	0.42	0.88	$0.551 \pm 0.024 \pm 0.024 \pm 0.026$
$Q^2 = 20 - 34 \text{ GeV}^2$			
0.023 – 0.040	0.031	0.89	$0.317 \pm 0.017 \pm 0.016 \pm 0.017$
0.040 – 0.060	0.050	0.89	$0.293 \pm 0.015 \pm 0.014 \pm 0.010$
0.060 – 0.090	0.075	0.89	$0.314 \pm 0.013 \pm 0.015 \pm 0.012$
0.090 – 0.120	0.10	0.88	$0.338 \pm 0.016 \pm 0.016 \pm 0.018$
0.120 – 0.160	0.14	0.88	$0.384 \pm 0.017 \pm 0.018 \pm 0.017$
0.160 – 0.205	0.18	0.88	$0.404 \pm 0.017 \pm 0.018 \pm 0.004$
0.205 – 0.260	0.23	0.88	$0.446 \pm 0.018 \pm 0.020 \pm 0.009$
0.260 – 0.330	0.29	0.87	$0.488 \pm 0.019 \pm 0.022 \pm 0.006$
0.330 – 0.400	0.36	0.87	$0.557 \pm 0.023 \pm 0.025 \pm 0.010$
0.400 – 0.467	0.42	0.87	$0.611 \pm 0.027 \pm 0.029 \pm 0.015$
0.467 – 0.556	0.49	0.87	$0.683 \pm 0.028 \pm 0.030 \pm 0.062$

Table 6: Measured values of F_2^γ/α and the applied radiative correction factors, \mathcal{R} , in bins of x for the three Q^2 ranges. The first uncertainty is statistic, the second systematic and the third is due to model dependence.

Q^2 range	$\langle Q^2 \rangle$	\mathcal{R}	F_2^γ/α
$x = 0.01 - 0.1$			
11 – 14	12.4	0.89	$0.278 \pm 0.006 \pm 0.028 \pm 0.013$
14 – 20	16.7	0.89	$0.287 \pm 0.006 \pm 0.015 \pm 0.015$
20 – 34	25.5	0.88	$0.316 \pm 0.008 \pm 0.016 \pm 0.013$
$x = 0.1 - 0.2$			
11 – 14	12.4	0.88	$0.377 \pm 0.010 \pm 0.039 \pm 0.008$
14 – 20	16.7	0.88	$0.355 \pm 0.009 \pm 0.017 \pm 0.005$
20 – 34	25.5	0.88	$0.399 \pm 0.011 \pm 0.019 \pm 0.010$
$x = 0.2 - 0.3$			
11 – 14	12.4	0.88	$0.464 \pm 0.015 \pm 0.051 \pm 0.009$
14 – 20	16.7	0.88	$0.442 \pm 0.013 \pm 0.020 \pm 0.003$
20 – 34	25.5	0.87	$0.477 \pm 0.015 \pm 0.023 \pm 0.013$
$x = 0.3 - 0.5$			
11-14	12.4	0.89	$0.544 \pm 0.017 \pm 0.061 \pm 0.019$
14-20	16.7	0.87	$0.545 \pm 0.014 \pm 0.024 \pm 0.012$
20-34	25.5	0.87	$0.594 \pm 0.015 \pm 0.029 \pm 0.022$

Table 7: The values of F_2^γ/α in bins of Q^2 for four x ranges together with the radiative correction factor. The first uncertainty is statistic, the second systematic and the third is due to model dependence.

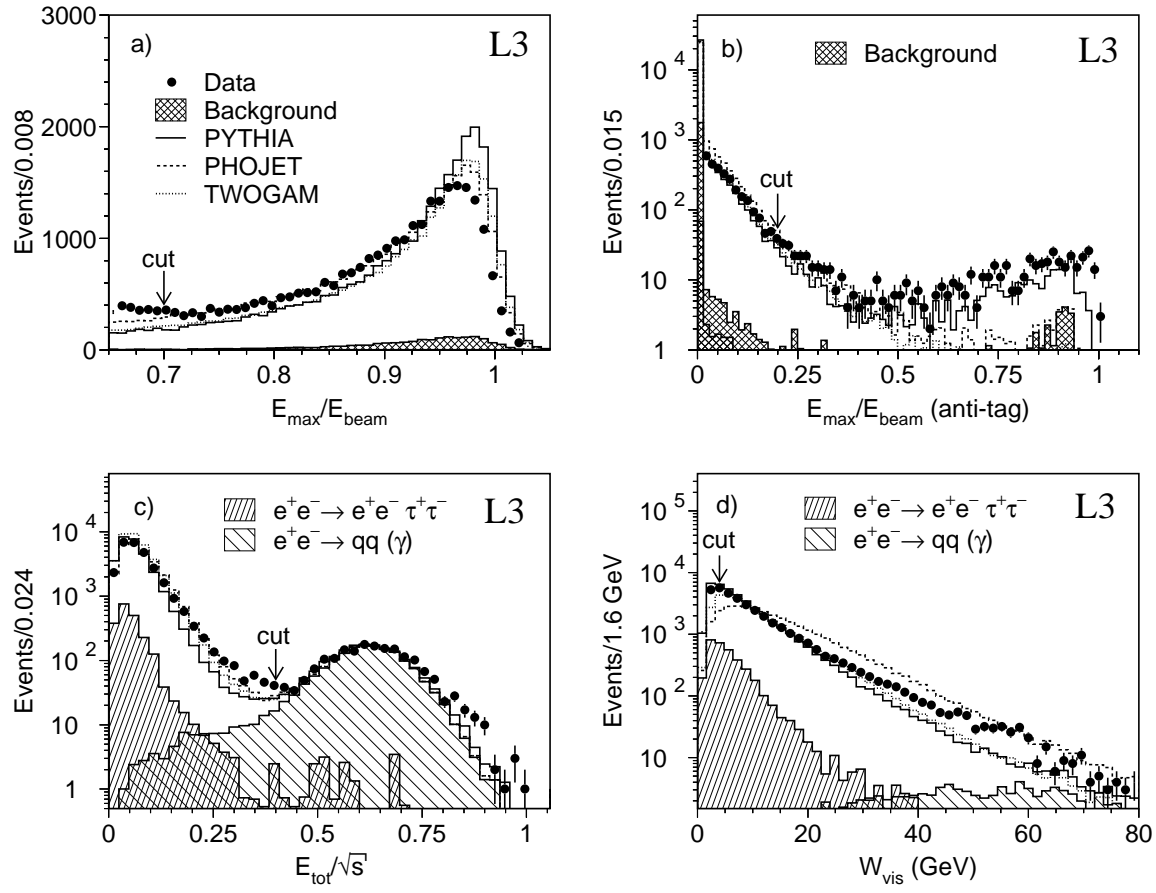


Figure 1: Distribution of the highest energy clusters in the forward electromagnetic calorimeters for a) the tagged electron side and b) for the opposite side. c) Total energy in the central calorimeters. d) The visible mass of the hadronic final state. All distributions are presented after all other cuts are applied. The backgrounds from annihilation and two-photon leptonic events are indicated as shaded areas and added to the expectations of the PYTHIA, PHOJET and TWOGAM generators. The arrows indicate the position of the cuts.

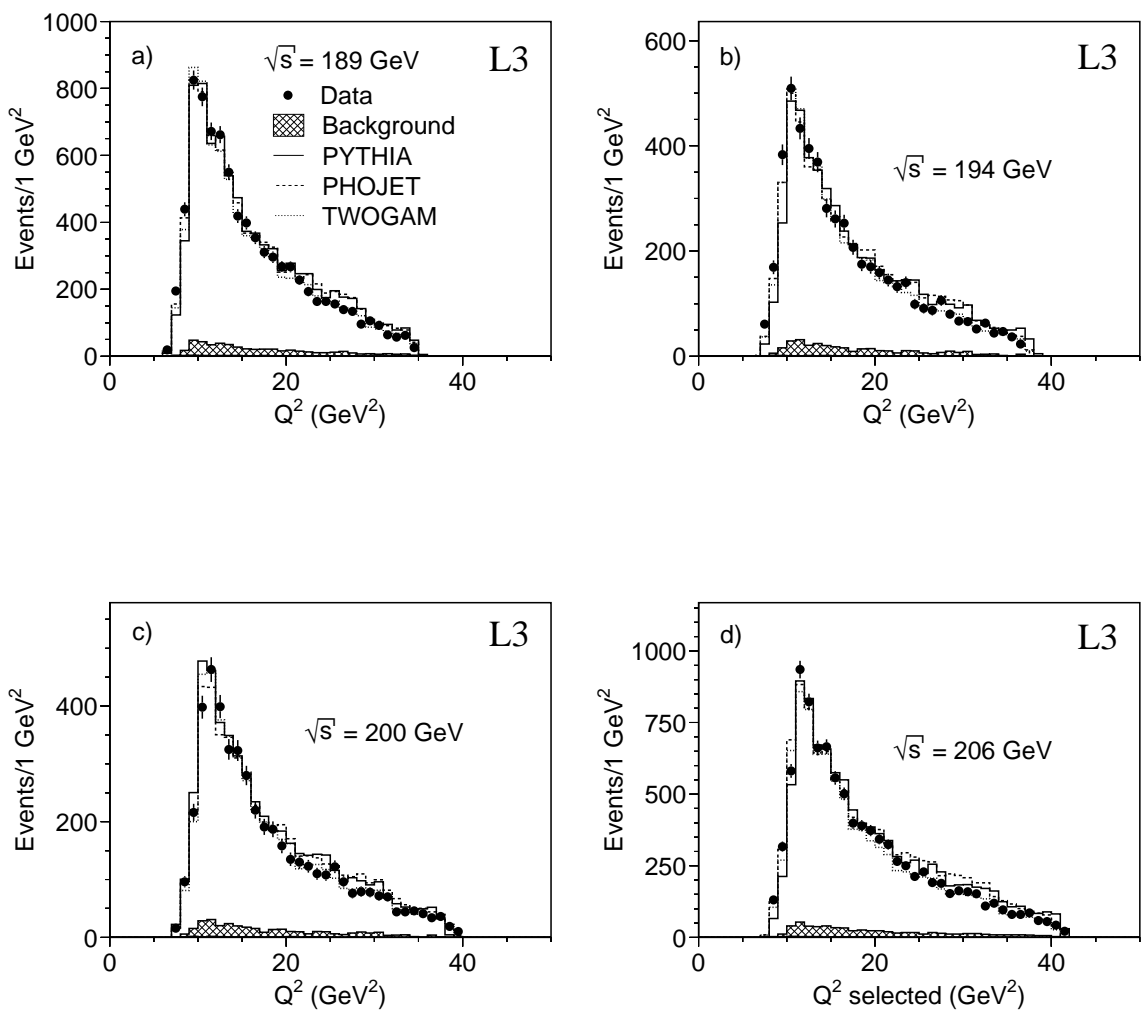


Figure 2: Q^2 distribution of the selected events for the four average \sqrt{s} ranges.

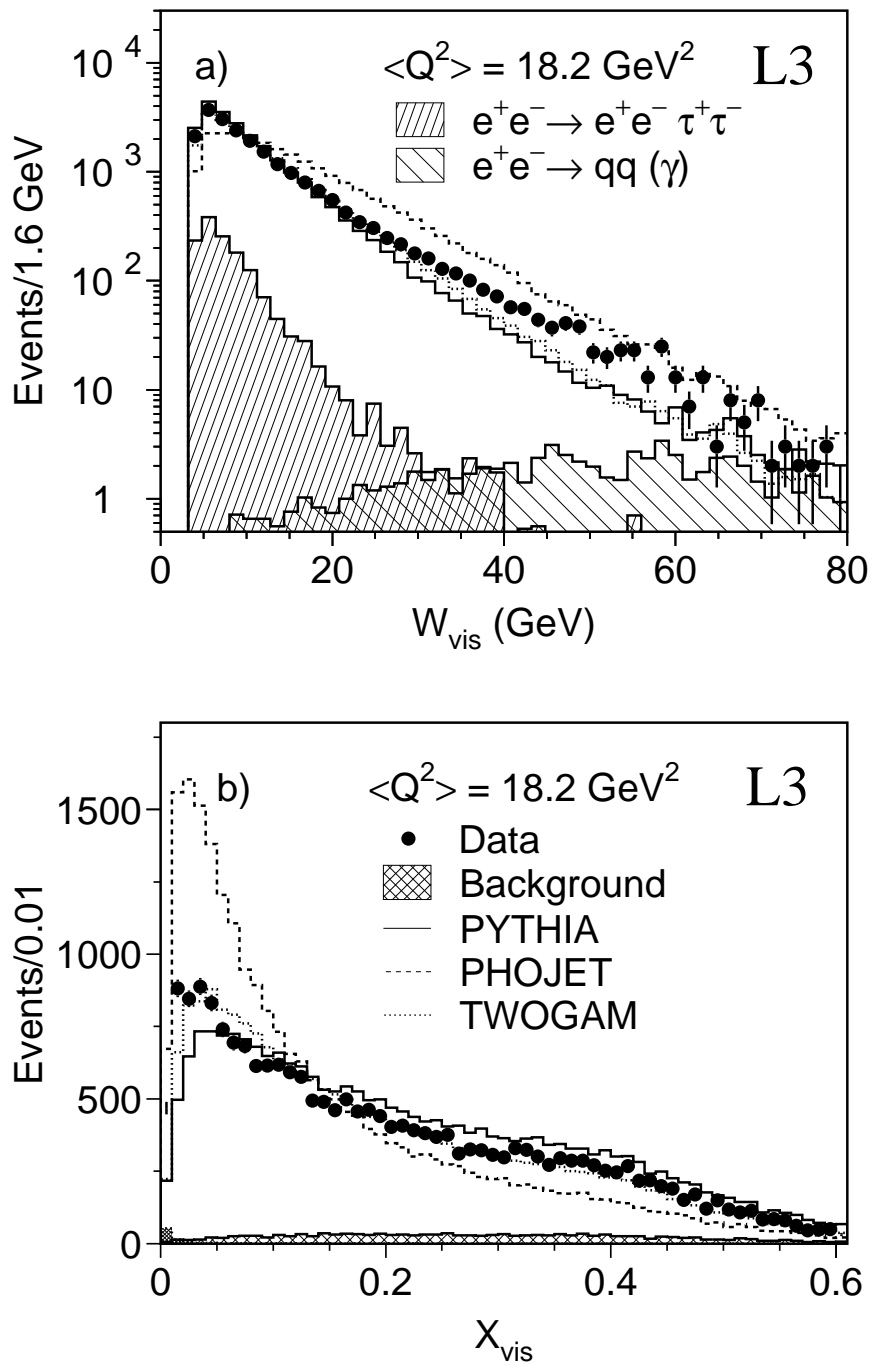


Figure 3: Distribution of the visible mass of the two-photon system and of the x_{vis} for all selected events compared with Monte Carlo predictions. The backgrounds from annihilation and two-photon leptonic events are indicated as shaded areas and added to the expectations of the PYTHIA, PHOJET and TWOGAM generators.

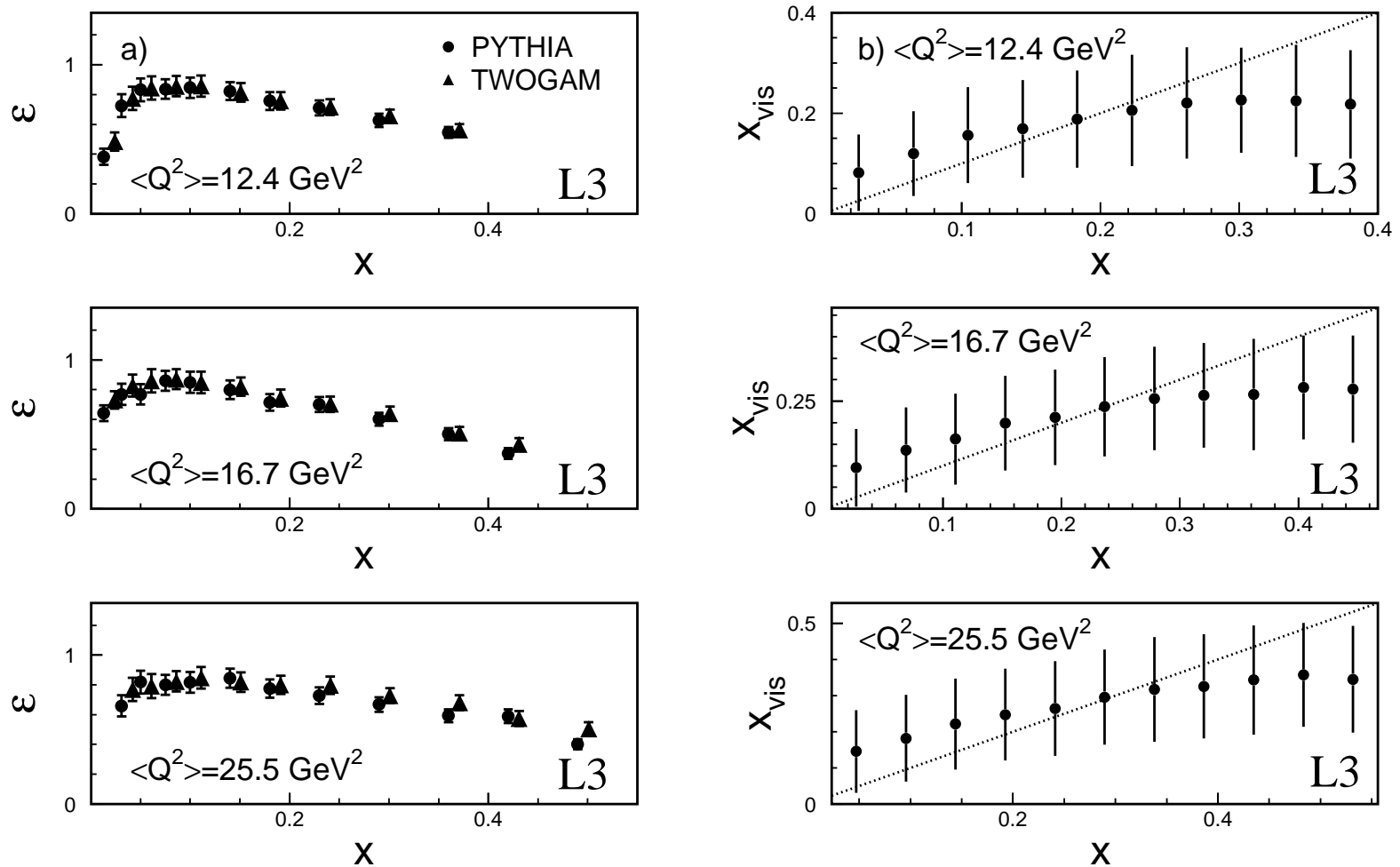


Figure 4: a) The detector acceptance and selection efficiency, ε , obtained by the PYTHIA and TWOGAM generators. b) Comparison of the reconstructed and generated value of x for the PYTHIA Monte Carlo at $\sqrt{s} = 189 \text{ GeV}$ for different values of Q^2 . The mean observed value and the standard deviation of x_{vis} are plotted for events generated in a given x bin.

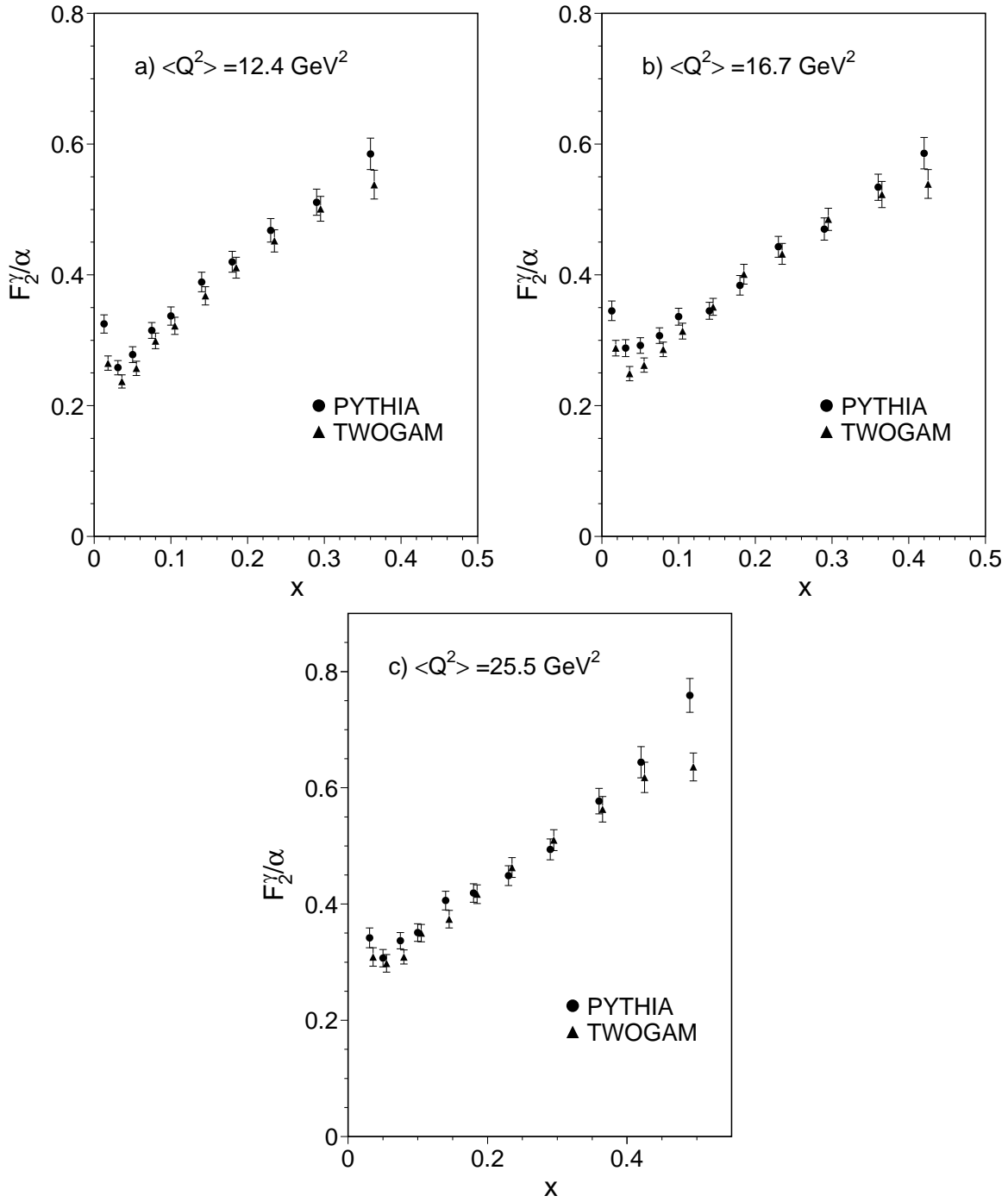


Figure 5: The photon structure function F_2^γ/α obtained with PYTHIA and TWOGAM. Only the statistical uncertainties are shown. For clarity, the symbols corresponding to the two Monte Carlo generators are slightly offset. The measurements are correlated as indicated in Tables 3 and 4

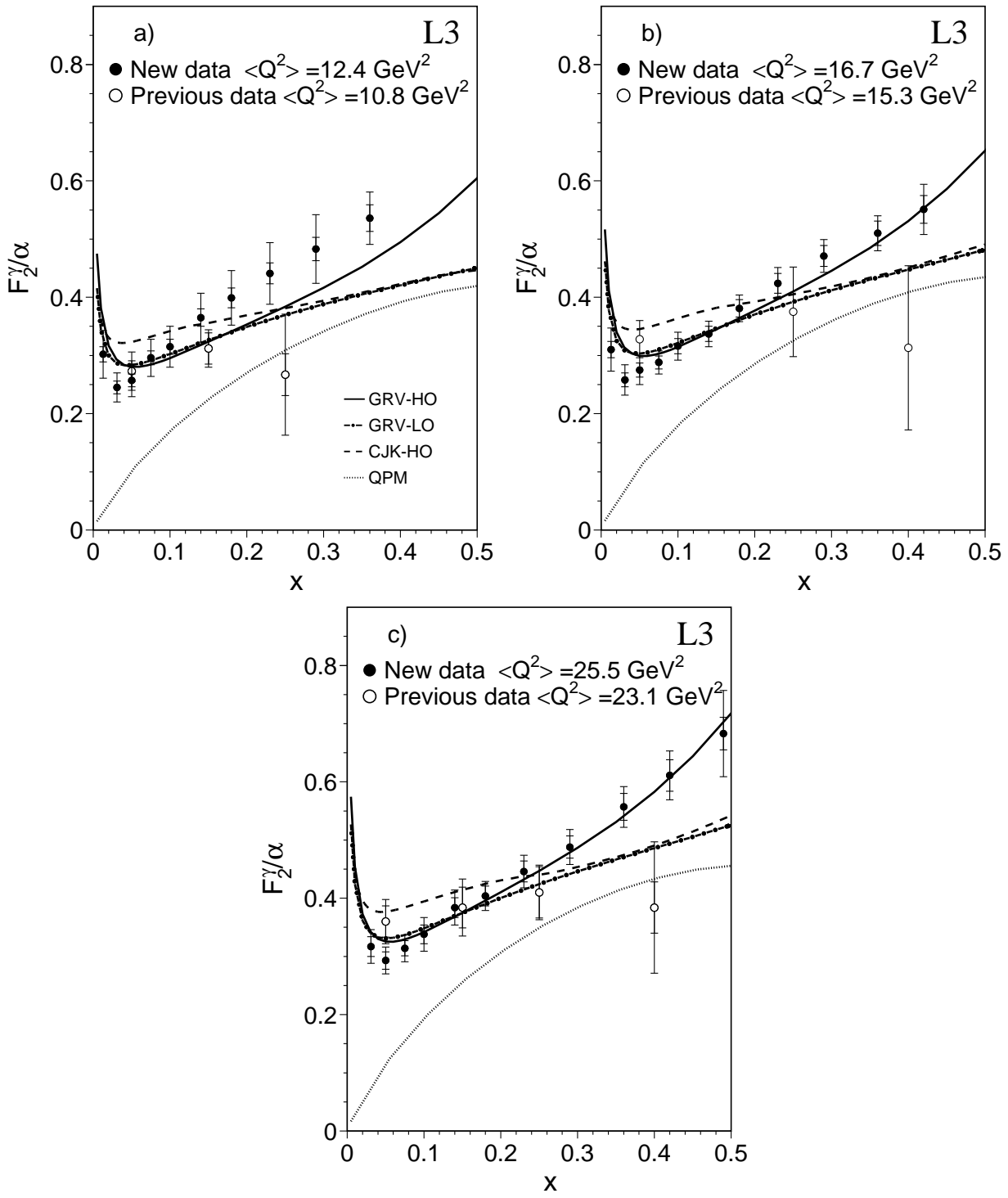


Figure 6: The photon structure function F_2^γ/α as a function of x for the three Q^2 intervals, with statistical and systematic uncertainties. The former are indicated by the inner error bars. The new data are presented together with the previous results at $\sqrt{s} = 183 \text{ GeV}$ [6]. The predictions of the higher-order parton density functions GRV and CJK are shown as well as the leading-order predictions of the GRV. The changes in slope of the CJK predictions are due to the c-quark threshold. The QPM predictions for $\gamma\gamma \rightarrow q\bar{q}$ are also shown.

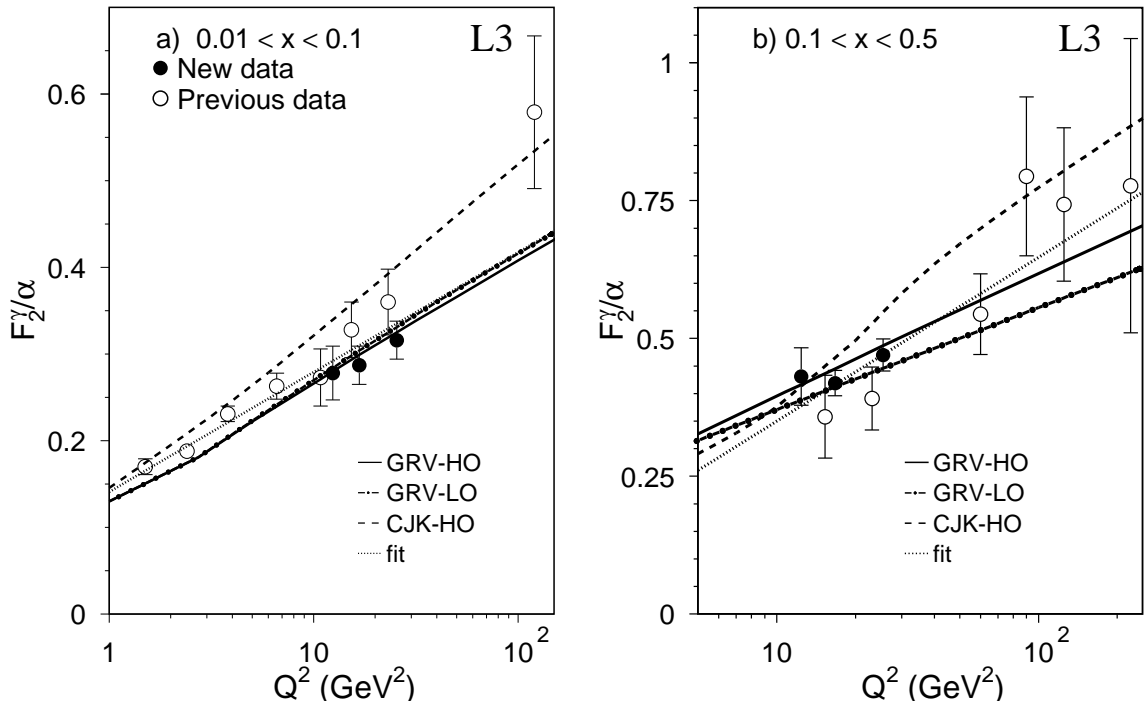


Figure 7: Evolution of the photon structure function F_2^γ/α as a function of Q^2 for two x intervals. The results of a fit to the data of the function $a + b(\ln Q^2 / \text{GeV}^2)$ are shown together with the predictions of the higher-order parton density functions GRV and CJK as well as the leading-order predictions of GRV.